Strojniški vestnik - Journal of Mechanical Engineering 70(2024)1-2, 42-54
DOI:10.5545/sv-jme.2023.692
Original Scientific Paper
Received for review: 2023-06-15
Received revised form: 2023-10-02
Accepted for publication: 2023-11-15

Multi-performance Optimization of the Rotary Turning Operation for Environmental and Quality Indicators

Tat-Khoa Doan[1], Trung-Thanh Nguyen[1], An-Le Van[2,*]
[1] Le Quy Don Technical University, Faculty of Mechanical Engineering, Vietnam
[2] Nguyen Tat Thanh University, Faculty of Engineering and Technology, Vietnam

In this investigation, two environmental metrics (the comprehensive energy used (TU) and turning noise (TN)) and a quality metric (surface roughness (SR)) of the rotary turning process for the Ti6Al4V were optimized and reduced using the optimal factors (the inclined angle-i, depth of cut-d, feed-f, and turning speed-V). The TU model was proposed comprising the embodied energy of the insert and lubricant. The method based on the removal effects of criteria (MEREC), an improved quantum-behaved particle swarm optimization algorithm (IQPSO), and TOPSIS were applied to select weight values and the best optimal solution. The machining cost (MC) was proposed in terms of process parameters. The outcomes presented that the optimal values of the i, d, f, and V were 35 deg., 0.30 mm, 0.40 mm/rev., and 190 m/min, respectively, while the TU, SR, TN, and MC were saved by 6.7 %, 22.3 %, 23.5 %, and 8.5 %, respectively. The turning responses were primarily affected by the feed rate and turning speed, respectively. The developed turning process could be employed for machining hard-to-cut alloys. The developed approach could be applied to deal with optimization problems for other machining operations.
Keywords: rotary turning, total energy consumption, surface roughness, noise emission, IQPSO

Highlights
- *A new rotary turning tool was designed and fabricated.*
- *Process parameters, including the spindle speed, depth of penetration, feed rate, and inclination angle were optimized.*
- *The total energy consumption, surface roughness, and turning noise were enhanced.*
- *An improved quantum-behaved particle swarm optimization algorithm was proposed.*

0 INTRODUCTION

The machining operation using rotary inserts is an effective solution to deal with hard-to-cut materials. The cutting temperature, force components, and pressure at the nose are reduced with the support of the rotational motion of the round piece. Additionally, a higher tool life is obtained due to the even distribution of the cutting temperature, leading to higher productivity and quality indicators, as compared to the conventional processes.

Different milling and turning operations having rotary inserts have been developed and optimized by many investigators. Karaguzel et al. [1] indicated that the rotary turning and milling processes provide 10- and 40-times longer tool life than conventional operations. The optimal cutting speed, feed, depth of cut, and inclination angle were selected to decrease the surface roughness and improve the material removal rate [2]. The ultrasonic vibration-based rotary turning was developed to machine decrease the machining forces and average roughness of the turned AA 7075 [3]. The results indicated the tool speed of 98.63 m/min and the feed of 0.08 mm/min were optimal data. A simulation model was developed to predict the tool wear in the rotary turning [4]. The authors stated that the tool wear was effectively decreased due to the disengagement duration. The energy efficiency and surface roughness were enhanced by 8.9 % and 24.8 %, respectively using the optimal process parameters [5]. Nguyen emphasized that the energy consumption, surface roughness, and material removal rate of the turned SKD11 were affected by the speed, feed, depth of cut, and inclination angle [6]. Umer et al. indicated that an increased speed and/or depth caused a higher temperature of the turned 51200 steel [7]. Ahmed et al. stated that surface roughness and tool wear of the turned AISI 4140 were decreased by 24.6% and 32.6 %, respectively using optimal process parameters [8].

Nieslony et al. [9] indicated that a higher speed caused a decrease in the surface roughness and a stable turning operation, while an increased depth led to a higher intensity of the vibration. A rotary milling process was developed to machine the titanium alloy, in which a low speed was recommended to reduce the tool wear rate [10]. Ahmed et al. [11] emphasized that low process parameters (speed, feed, and depth of cut) and high inclination angle decreased the temperature of the rotary turning. Similarly, Chen et al. [12] emphasized that the surface roughness produced by the rotary process was lower than the conventional one. A novel simulation model was developed to forecast the temperature of the turned nickel and titanium alloys [13]. The authors stated that low process parameters

*Corr. Author's Address: Nguyen Tat Thanh University, 300A Nguyen Tat Thanh, Ho Chi Minh, Vietnam, lvan@ntt.edu.vn

(speed, feed, and depth of cut) and high inclination angle decreased the temperature. Umer et al. [14] revealed that a lower depth of cut was recommended to reduce the temperature and forces. The total energy consumed and machining time of the turned SKD61 were decreased by 17.0 % and 17.8 %, respectively, using the optimal factors [15]. Additionally, the carbon emission of the rotary turning operation was reduced by 5.0 % using the PSO [16]. He et al. revealed that the cutting temperature of the turned K417 alloy decreased with a higher inclination angle and cutting speed [17]. However, the shortcomings of the aforementioned works can be expressed as follows.

An efficient self-propelled rotary tool having high stiffness to machine high-hardness steels has not been designed and fabricated to replace the fixed turning one. Low rigidity is a primary drawback of the proposed tools in previous publications.

The noise emission damages the inner ear and causes occupational hearing loss as well as chronic stress; hence, minimizing the sound intensity of the rotary turning operation is a necessary requirement.

Moreover, the optimal process variables have not been determined to make reductions in energy consumed, roughness, and noise emission.

The next section presents the framework. The experimental setting and discussions are then shown. Finally, the obtained findings are drawn.

1 THE CONCEPT OF THE ROTARY TURNING OPERATION

The principle of the rotary turning process to produce external surfaces of hardened materials is presented in Fig. 1a. The workpiece is rotated around its axis, while the motion of the round piece is conducted using the friction between the body and specimen. The manufactured tool is shown in Fig. 1b, including the screws, bolts, the round insert, the base, and the holder. The milled grooves on the base are utilized to change the inclination angle. The round insert is conducted self-rotation using two bearings. The round inserts having a rake angle of 11° and a hardness of 92 HRC are utilized for all tests.

2 OPTIMIZATION APPROACH

The *TU* consists of the turning energy (*TE*), embodied energy for the insert (*EI*), and embodied energy for the coolant (*EC*).

$$TU = TE + EI + EC. \tag{1}$$

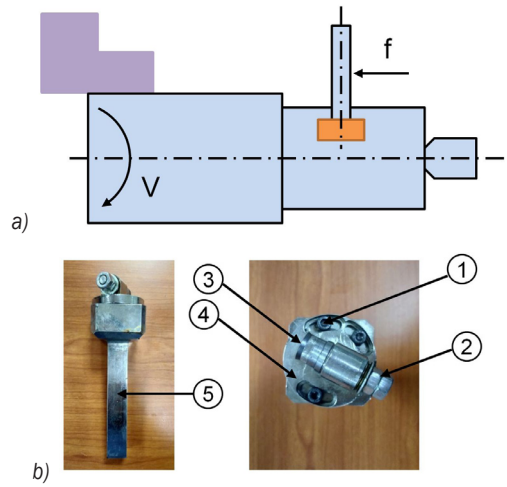

Fig. 1. *The concept of the rotary turning process; a) the schematic principle, and b) the fabricated rotary tool (1. the screws; 2. the bolts; 3. the round insert, 4. the base; and 5. the holder)*

The *EC* is computed as:

$$TE = E_{st} + E_{sb} + E_{tn} + E_{at} + E_t + E_{tc}, \tag{2}$$

where E_{st}, E_{sb}, E_{tn}, E_{at}, E_t, E_{tc} are energy consumed in the startup, standby, transition, air-turning, turning, and tool change stages (Fig. 2).

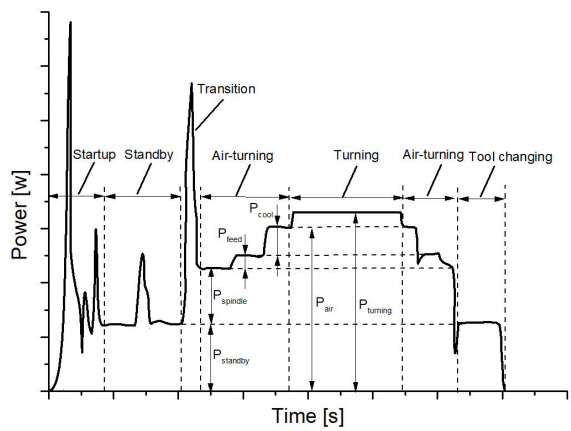

Fig. 2. *The machining load of the rotary turning process*

The start-up state presents the shortest period for turning on the lathe. The standby state denotes the stable period, which starts with turning on the machine tool and stops with the spindle rotation. The transition state refers to the short period for increasing and decreasing the spindle speed. The air-turning state presents the duration with spindle rotation but no material cutting. The turning state refers to the steady period for material removal.

$$TE = P_o t_o + P_{sb} t_{sb} + aV^2 + bV + c + (P_{st} + c_1 V + c_2) t_a + P_c t_c + P_{st} t_{tc} \left(\frac{t_c}{T_T} \right), \quad (3)$$

where P_o, P_{sb}, and P_c are the power used in the startup, standby, and turning states, respectively. t_o, t_{sb}, t_a, and t_c are the startup, standby, air-cutting, and turning time, respectively. a, b, and c denote the experimental coefficients. t_{tc} and T_T are the tool change time and tool life, respectively. The T_T is expressed as:

$$T_T = \frac{A}{V^\alpha f^\beta d^\gamma}, \quad (4)$$

where A, α, β, and γ are the experimental coefficients.

The *EI* is computed as:

$$EI = \frac{t_c}{T_T} SE_i I_v, \quad (5)$$

where SE_i and I_v are the fabricating energy and volume of each insert, respectively.

The *EC* is computed as:

$$EC = \frac{t_c}{T_L} V_u \eta \rho E_L, \quad (6)$$

where T_L and E_L denote the cycle time and fabricating energy of the lubricant, respectively. V_u is the lubricant volume. ρ and η are the density and concentration of the lubricant, respectively.

The *SR* is computed as:

$$SR = \sum_{i=1}^{n} \frac{R_{ai}}{n}, \quad (7)$$

where R_{ai} is the average roughness at the i_{th} measured point.

The *TN* is computed as:

$$TN = \sum_{i=1}^{n} \frac{TN_i}{n}, \quad (8)$$

where TN_i is the turning noise at the i^{th} measured time.

In this study, the characteristics of the coolant system, cutting piece, and specimen are named as constants. The factors considered and their levels are presented in Table 1. The ranges are determined based on the specifications of the lathe. Moreover, these values are confirmed with the published works related to the rotary turning processes. The optimization issue is presented as:

Find $X = [i, V, f, \text{and } d]$.
Minimizing *TU*, *SR*, and *TN*;
Constraints: 20 deg $\leq i \leq$ 50 deg;
0.3 mm $\leq d \leq$ 0.7 mm;
0.4 mm/rev $\leq f \leq$ 0.8 mm/rev;
90 m/min $\leq V \leq$ 190 m/min.

Table 1. *Process parameters of the rotary turning*

Symbol	Parameters	1	2	3
i	Inclination angle [deg]	20	35	50
d	Turning depth [mm]	0.3	0.5	0.7
f	Feed rate [mm/rev]	0.4	0.6	0.8
V	Turning speed [m/min]	90	140	190

3.2 Optimization Framework

The optimizing approach is depicted in Fig. 3.

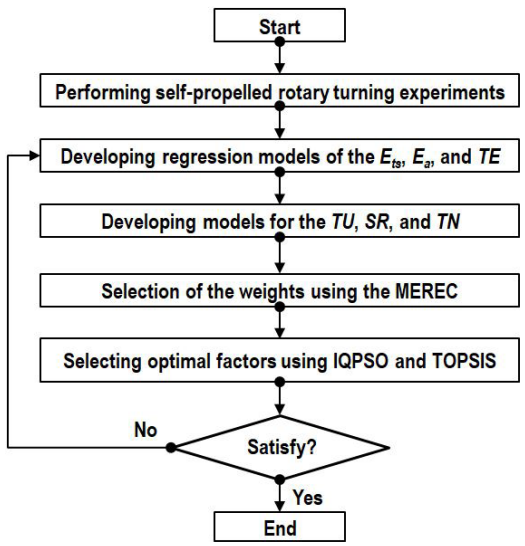

Fig. 3. *Systematic optimizing procedure*

Step 1: Performing experimental tests using the Box-Behnken design [18] and [19].

The Box-Behnken design requires three levels for each factor, which presents the lowest, middle, and highest ranges. The design points are placed on the middle points of the edge and the centre of the block. The advantages of the Box-Behnken design are the low number of tests and ensuring predictive accuracy. The number of experiments (*NE*) in the Box-Behnken design is computed as [20]:

$$NE = 2n(n-1) + N_c, \quad (9)$$

where n and N_c are the number of variables and the number of centre points, respectively. In this work, 29 experiments are performed for 4 process parameters and 5 replications.

Step 2: Developing regression models for energy components, *SR*, and *TN* [21].

Step 3: The MEREC is utilized to compute the weights.

For the maximizing aim, the normalized response (n_{ij}) is computed as:

$$n_{ij} = \frac{\min y_i}{y_i}. \tag{10}$$

For the minimizing aim, the n_{ij} is computed as:

$$n_{ij} = \frac{y_i}{\max y_i}. \tag{11}$$

The performance of the alternatives S_i is computed as:

$$S_i = \ln\left[1+\left(\frac{1}{n}\sum_j \left|\ln(n_{ij})\right|\right)\right], \tag{12}$$

where n is the number of responses.

The performance of i^{th} alternative is computed as:

$$S'_{ij} = \ln\left[1+\left(\frac{1}{n}\sum_{k,k\neq j} \left|\ln(n_{ij})\right|\right)\right]. \tag{13}$$

The removal effect of the j^{th} response (E_j) is computed as:

$$E_j = \sum i \left|S'_{ij} - S_i\right|. \tag{14}$$

The weight (ω_i) is computed as:

$$\omega_i = \frac{E_j}{\sum_k E_k}. \tag{15}$$

Step 4: Generation of the optimality using the IQPSO.

In the QPSO, the updated position of each particle is expressed as: **[22]** and **[23]**:

$$x_{i,j}(t+1) = p_{i,j}(t) - \alpha(m_{best\,i,j}(t) - x_{i,j}(t))\ln\left(\frac{1}{u}\right) \quad \text{If } k \geq 0.5, \tag{16}$$

$$x_{i,j}(t+1) = P_{i,j}(t) + \alpha\left(m_{best\,i,j}(t) - x_{i,j}(t)\right)\ln\left(\frac{1}{u}\right) \quad \text{If } k < 0.5, \tag{17}$$

$$p_{i,j}(t+1) = \lambda P_{i,j}(t) + (1-\lambda)G_j(t), \tag{18}$$

$$m_{best\,i,j}(t) = \frac{1}{N}\sum_{i=1,j=1}^{N,M} P_{i,j}(t). \tag{19}$$

In this work, the IQPSO combining the QPSO and theCauchy-Lorentz distribution is proposed to expand the perturbation **[24]**. The probability density function ($f(x)$) of the Cauchy-Lorentz distribution is given as:

$$f(x, x_o, \gamma) = \frac{1}{\pi}\left(\frac{\lambda}{(x-x_o)^2+\gamma^2}\right), \tag{20}$$

where x_o and γ are the locations of the peak of the distribution and scale parameter, respectively.

In the mutation stage, each vector is added by a Cauchy-Lorentz random value ($D(.)$) and expressed:

$$x' = x + \lambda D(.), \tag{21}$$

where x' is the new location after mutatation with random value to x.

The convergence of the QPSO-CL is enhanced with the aid of natural selection, which is expressed as:

$$F(X(t)) = \{F(x_1(t)), ..., F(x_N(t))\}, \tag{22}$$

where $X(t)$ and $F(X(t))$ are the position vector of particles and fitness function of swarm, respectively. The particles are sorted based on fitness values, which is expressed as:

$$F(X'(t)) = \{F(x_1'(t))...F(x_N'(t))\},$$
$$X'(t) = \{x_1'(t), ...x_N'(t)\}, \tag{23}$$

The operating steps of the IQPSO are illustrated in Fig. 4. Matlab 2019 commercial software entitled is used to conduct the IQPSO.

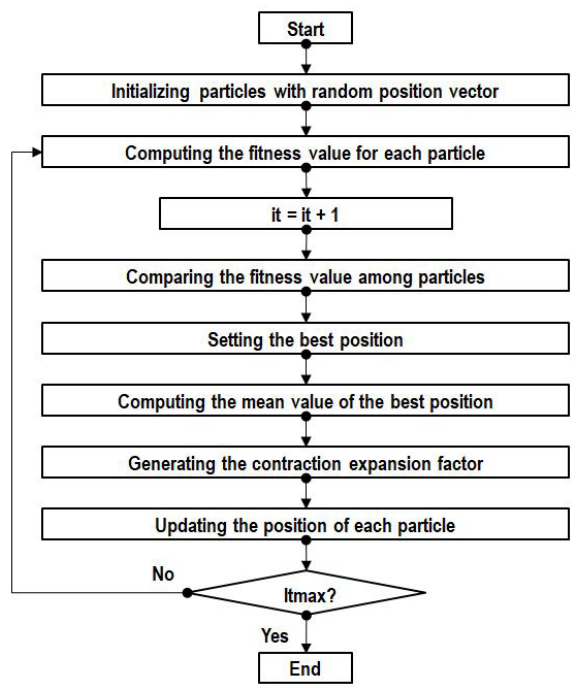

Fig. 4. *The operating procedure of the IQPSO*

Step 4: The best solution is selected by the TOPSIS.

The normalized value of each alternative (g_{ij}) is computed as:

$$g_{ij} = \frac{e_{ij}}{\sqrt{\sum_{i=1}^{m} e_{ij}^2}}, \quad (24)$$

where e_{ij} presents the value of the alternative j_{th}.

The positive ideal solution (P^+) and the negative idea solution (N^-) are computed as:

$$P^+ = \sqrt{\sum_{j=1}^{m} \left(v_{ij} - v_j^+\right)^2}, \quad (25)$$

$$N^- = \sqrt{\sum_{j=1}^{m} \left(v_{ij} - v_j^-\right)^2}. \quad (26)$$

The best point is found with the highest selection index (S_i), which is calculated as:

$$S_i = \frac{N^-}{P^+ + N^-}. \quad (27)$$

3 EXPERIMENTAL SETTING

A turning machine entitled EMCOTURN E45 is utilized to execute the turning trials. The Ti6Al4V bar with an outside diameter of 60 and a length of 400 mm is utilized as the specimen (Fig. 5). The chemical compositions of the Ti6Al4V produced by EDX results are presented in Table 2 and Fig. 6. The outside diameter, inside diameter, and thickness of the round insert are 12 mm, 4.4 mm, and 4.76 mm, respectively. A KEW6305 electrical sensor, Mitutoyo SJ-301, and EXTECH 407730 sound meter are employed to obtain the power components, machined roughness, and turning noise.

Fig. 5. *The turned specimens*

Table 2. *Chemical compositions of the Ti6Al4V*

Elements	Al	Ti	V	Fe	C	O	Others
[%]	6.01	83.74	3.26	0.16	0.28	5.08	Allowance

The representative data of the rotary turning operation are depicted in Fig. 7. Fig. 7a presents the power used at the experimental No. 16, while the roughness profile and SEM image are shown in Figs. 7b and c, respectively. The wear and fracture have not been found on the edges of round inserts, as shown in Fig. 7d. The noise profile is presented in Fig. 7e.

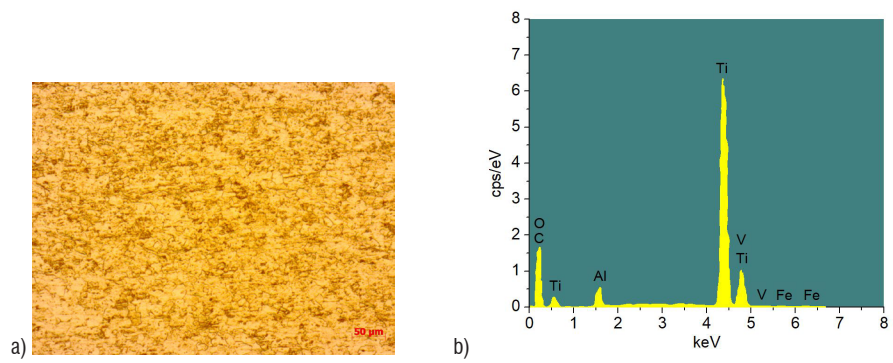

Fig. 6. *Investigation of a) the microstructure, and b) chemical compositions of Ti6Al4V; produced by EDX results*

Table 3. *Regression models of the energy consumed in the transition state and operational power*

No.	Regression model	R^2	Adjusted R^2	Predicted R^2
1	$EC_{ts} = 0.000025V^2 - 0.0014V + 0.4682$	0.9882	0.9794	0.9654
2	$P_{op} = 0.0025V + 0.03682$	0.9924	0.9826	0.9758

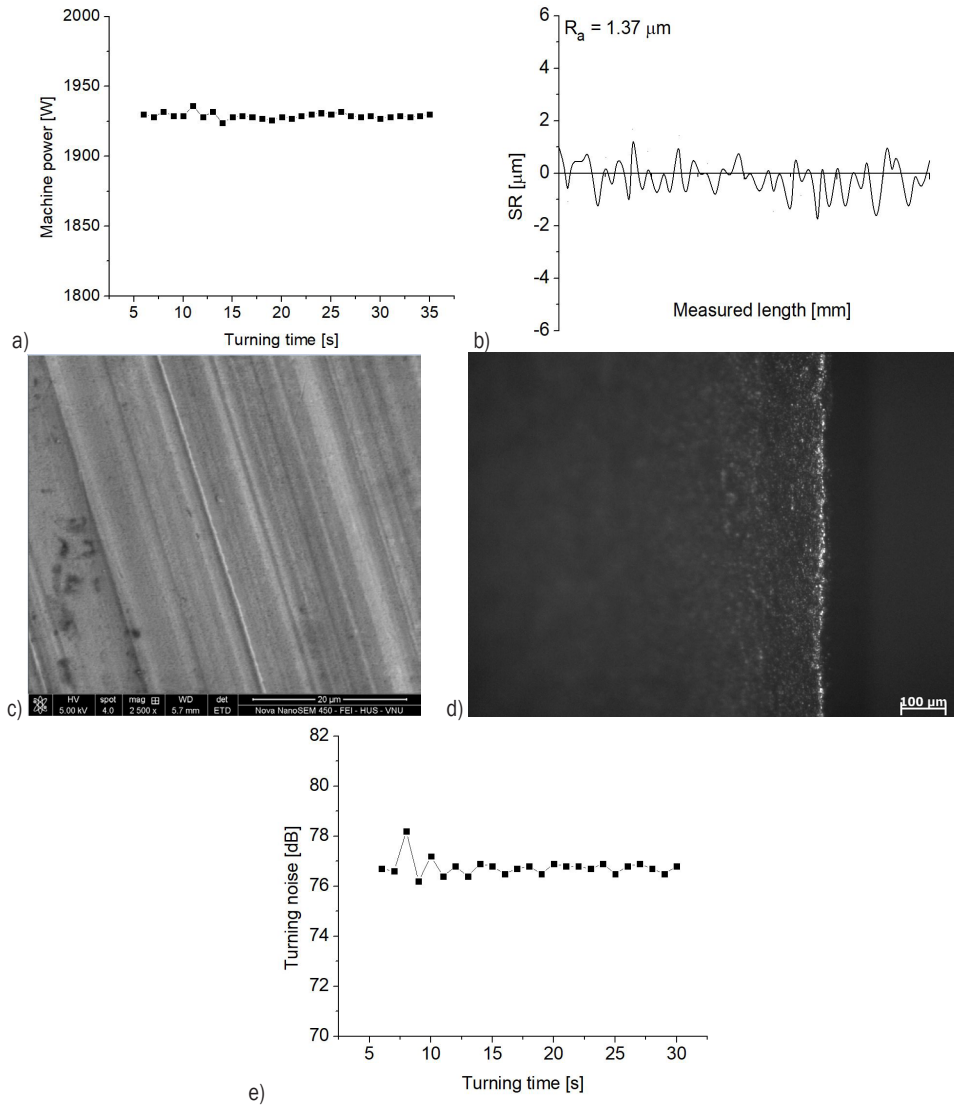

Fig. 7. *Representative experiments at experimental No. 16; a) power consumed, b) average roughness, c) the SEM image, d) the SEM image of the round insert, e) turning noise*

4 RESULTS AND DISCUSSIONS

4.1 Development of EC_{ts} and P_{op} Models

The EC_{ts} and P_{op} models are shown in Table 3.

4.2 Development of E_t, *SR*, and TN models

The obtained data for the E_t, *SR*, and *TN* are presented in Table 4.

The ANOVA results of the E_t, *SR*, and *TN* are shown in Tables 5 to 7, respectively. The values of the R^2, the adjusted R^2, and the predicted R^2 values indicate that the E_t, *SR*, and *TN* correlations are significant.

For the E_t model, the contributions of the *i*, *d*, *f*, and *V* are 2.11 %, 6.04 %, 22.79 %, and 27.33 %, respectively. The contributions of the *if*, *df*, *dV*, and *fV* are 1.22 %, 2.44 %, 2.89 %, and 4.23 %, respectively. The contributions of the i^2, f^2, and V^2 are 6.89 %, 9.33 %, and 13.2 %, respectively.

For the *SR* model, the contributions of the *i*, *d*, *f*, and *V* are 6.37 %, 18.18 %, 22.15 %, and 23.36 %, respectively. The contributions of the *id*, *iV*, *dV*, and *fV* are 1.06 %, 2.42 %, 3.34 %, and 2.59 %, respectively. The contributions of the i^2 and d^2 are 15.22 % and 3.38 % respectively.

For the *TN* model, the contributions of the *i*, *d*, *f*, and *V* are 17.37 %, 15.91 %, 16.82 %, and 18.09 %, respectively. The contributions of the *if*, *dV*, and *fV* are 1.64 %, 1.44 %, and 1.04 %, respectively. The contributions of the i^2, d^2, f^2, and V^2 are 21.23 %, 1.82 %, 1.35 %, and 2.22 % respectively.

The deviations between the actual and predictive values of the E_t, *SR*, and *TN* change from –0.99 % to 1.26 %, from –0.97 to 0.80, and –1.26 % to –0.47 %, respectively (Table 8). Therefore, the E_t, *SR*, and *TN* models are significant.

The probability plots of three responses are presented in Fig. 8. It can be stated that observed data are distributed on straight lines, indicating the goodness of the fit of the proposed models.

Table 4. *Experimental data for developing the E_t, SR, and TN models*

No.	*i*	*d*	*f*	*V*	E_t	*SR*	*TN*
Experimental data for developing models							
1	50	0.5	0.6	190	8.75	2.17	98.1
2	20	0.3	0.6	140	9.69	2.04	78.2
3	35	0.3	0.8	140	7.57	2.24	78.2
4	20	0.5	0.8	140	8.67	2.78	91.4
5	50	0.5	0.4	140	14.90	2.16	79.4
6	20	0.7	0.6	140	10.78	2.75	92.1
7	50	0.5	0.6	90	15.73	2.99	81.4
8	35	0.7	0.4	140	14.24	2.19	73.3
9	20	0.5	0.4	140	13.98	1.97	77.4
10	35	0.5	0.6	140	9.60	2.18	76.3
11	50	0.3	0.6	140	9.99	2.31	80.1
12	35	0.5	0.4	90	19.34	2.14	59.8
13	20	0.5	0.6	190	8.36	1.81	96.5
14	35	0.5	0.6	140	9.62	2.16	76.8
15	35	0.3	0.4	140	12.08	1.41	58.8
16	35	0.5	0.4	190	11.47	1.37	76.7
17	35	0.5	0.8	190	6.52	2.11	94.9
18	35	0.7	0.6	190	8.52	2.22	93.4
19	50	0.5	0.8	140	8.99	3.02	96.7
20	50	0.7	0.6	140	11.29	2.94	94.2
21	35	0.5	0.8	90	12.32	3.07	75.9
22	35	0.3	0.6	190	7.55	1.49	77.3
23	20	0.5	0.6	90	15.09	2.81	79.2
24	35	0.7	0.6	90	15.56	2.94	74.1
25	35	0.7	0.8	140	8.53	2.99	91.4
26	35	0.3	0.6	90	13.18	2.46	60.9
Experimental data for testing developed models							
27	25	0.5	0.4	100	17.72	2.15	65.7
28	30	0.4	0.5	120	14.57	2.17	63.3
29	40	0.6	0.7	140	8.95	2.63	85.7
30	25	0.7	0.5	130	13.08	2.51	80.7
31	40	0.5	0.7	150	8.11	2.36	84.3
32	45	0.4	0.6	160	8.73	2.06	81.9

Table 5. *ANOVA results for the E_t model*

So.	SS	MS	*F*-value	*p*-value	Con. [%]
Mo.	249.1	17.8	35.6	< 0.0001	
i	37.4	37.4	74.8	0.003	2.11
d	107.1	107.1	214.1	< 0.0001	6.04
f	404.0	404.0	807.9	< 0.0001	22.79
V	484.4	484.4	968.9	< 0.0001	27.33
if	21.6	21.6	43.2	0.007	1.22
dV	51.2	51.2	102.5	0.003	2.89
fV	75.0	75.0	150.0	0.002	4.23
i^2	122.1	122.1	244.3	< 0.0001	6.89
f^2	165.4	165.4	330.8	< 0.0001	9.33
V^2	234.0	234.0	467.9	< 0.0001	13.2
Re.	5.5	0.5			
To.	254.6				
R^2 = 0.9784; Adj. R^2 = 0.9692; Pred. R^2 = 0.9578					

Table 6. *ANOVA results for the SR model*

So.	SS	MS	*F*-value	*p*-value	Con. [%]
Mo.	6.33	0.45	38.90	< 0.0001	6.37
i	0.42	0.42	154.86	< 0.0001	18.18
d	1.19	1.19	441.98	< 0.0001	22.15
f	1.45	1.45	538.49	< 0.0001	23.36
V	1.53	1.53	567.91	< 0.0001	1.06
id	0.07	0.07	25.77	0.010	6.37
iV	0.16	0.16	58.83	0.007	2.42
dV	0.22	0.22	81.20	0.009	3.34
fV	0.17	0.17	62.97	0.007	2.59
i^2	1.00	1.00	370.02	< 0.0001	15.22
d^2	0.22	0.22	82.17	0.009	3.38
Re.	0.13	0.01			
To.	6.45				
R^2 = 0.9802; Adj. R^2 = 0.9784; pred. R^2 = 0.9662					

Table 7. ANOVA results for the *TN* model

So.	SS	MS	*F*-value	*p*-value	Con. [%]
Mo.	3168.7	226.3	44.4	< 0.0001	
i	2729.5	2729.5	535.1	0.0010	17.37
d	2500.1	2500.1	490.1	< 0.0001	15.91
f	2643.0	2643.0	518.1	< 0.0001	16.82
V	2842.6	2842.6	557.3	< 0.0001	18.09
if	257.7	257.7	50.5	0.0068	1.64
dV	226.3	226.3	44.4	0.0075	1.44
fV	163.4	163.4	32.0	0.0078	1.04
i^2	3336.0	3336.0	654.0	< 0.0001	21.23
d^2	286.0	286.0	56.1	0.0066	1.82
f^2	212.1	212.1	41.6	0.0074	1.35
V^2	348.8	348.8	68.4	0.0062	2.22
Re.	56.1	5.1			
To.	3224.8				
R^2 = 0.9826; Adj. R^2 = 0.9794; pred. R^2 = 0.9685					

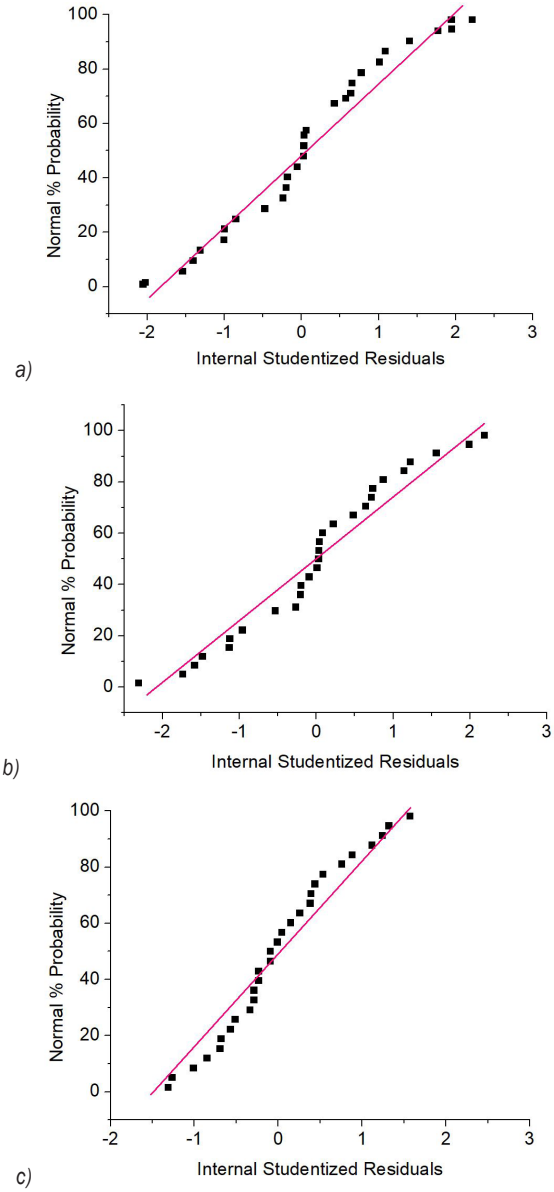

Fig. 8. *The probability plots of three responses; a) for E_t model, b) for SR model, c) for TN model*

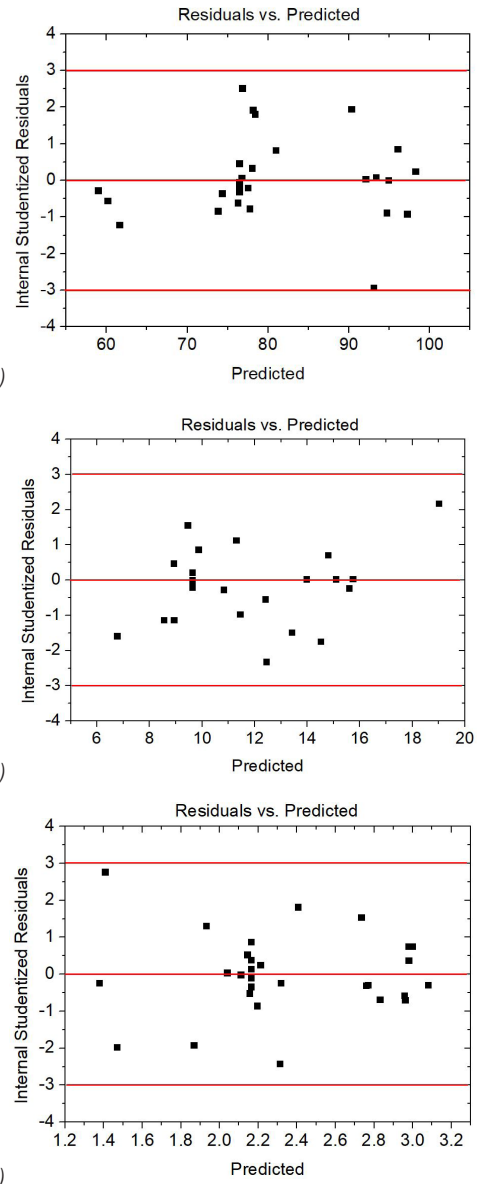

Fig. 9. *The residuals versus the observations for three responses; a) for E_t model, b) for SR model, c) for TN model*

The residuals versus the observations of three responses are presented in Fig. 9. The errors of the responses are systematically distributed, presenting constant errors for each model.

4.3 Parametric Impacts

The E_t is first reduced by 2.8 % with a higher i (Fig. 10a). However, the E_t is increased by 7.9 % with a further i. An increased i causes a reduction in the cutting volume, leading to a decrease in the resistance; hence, the E_t reduces. A higher i increases the cutting volume due to the perpendicular tool, resulting in higher friction; hence, the E_t increases.

The E_t is increased by 14.9 % with an increment in the d (Fig. 10a). A higher d increases the thickness of the chip; hence, the E_t increases.

The E_t is decreased by 33.6 % with an increment in the f (Fig. 10b). A higher f reduces the turning time; hence, the E_t increases.

The E_t is decreased by 38.9 % with an increment in the V (Fig. 10b). When the V increases, the turning time reduces; hence, the energy consumption decreases.

Table 8. *Confirmations of the precision of the developed models*

No.	E_t [kJ]			SR [μm]			TN [dB]		
	Exp.	Pred.	Err.	Exp.	Pred.	Err.	Exp.	Pred.	Err.
27	17.72	17.86	-0.79	2.15	2.16	-0.47	65.7	66.1	-0.61
28	14.57	14.62	-0.34	2.17	2.18	-0.46	63.3	64.1	-1.26
29	8.95	9.04	-1.01	2.63	2.62	0.38	85.7	86.1	-0.47
30	13.08	13.16	-0.61	2.51	2.49	0.80	80.7	81.2	-0.62
31	8.11	8.19	-0.99	2.36	2.38	-0.85	84.3	84.9	-0.71
32	8.73	8.62	1.26	2.06	2.08	-0.97	81.9	82.6	-0.85

The *SR* is first decreased by 11.2 % with an increment in the *i* (Fig. 11a). However, the *SR* is increased by 21.9 % with a further *i*. An increased *i* decreases the turning volume, resulting in a low resistance; hence, a low *SR* is produced. A higher i causes an increased turning volume, leading to a hard turning; hence, a rough surface is generated.

The *SR* is increased by 30.9 % with a higher *d* (Fig. 11a). A higher *d* causes an increase in the turning volume, leading to higher resistance; hence, a higher *SR* is produced.

The *SR* is increased by 47.6 % with an increment in the *f* (Fig. 11b). A higher *f* causes an increase in the turning volume, leading to a higher friction; hence, the SR increases. Moreover, A higher f causes an increase in the turning marks, resulting in a higher roughness.

The *SR* is decreased by 47.6 % with an increment in the *V* (Fig. 11b). The cutting temperature increases with an increment in the *V*, resulting in softer specimen; hence, the *SR* reduces.

The *TN* is decreased by 8.72 % with an increment in the *i* (Fig. 12a). However, the *TN* is increased by 47.5 % with further *i*. A higher *i* decreases the material removal volume, resulting in low friction between the turning insert and workpiece; hence, the *TN* decreases. In contrast, a further *i* increases the material removal volume, leading to greater resistance; hence, the *TN* increases.

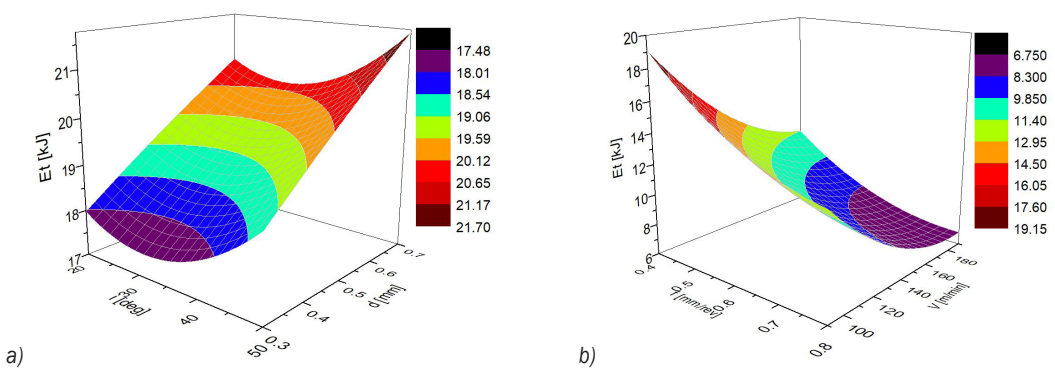

a) b)

Fig. 10. *Interactions of process parameters on the E_t; a) E_t vs. i and d, b) E_t vs. V and f*

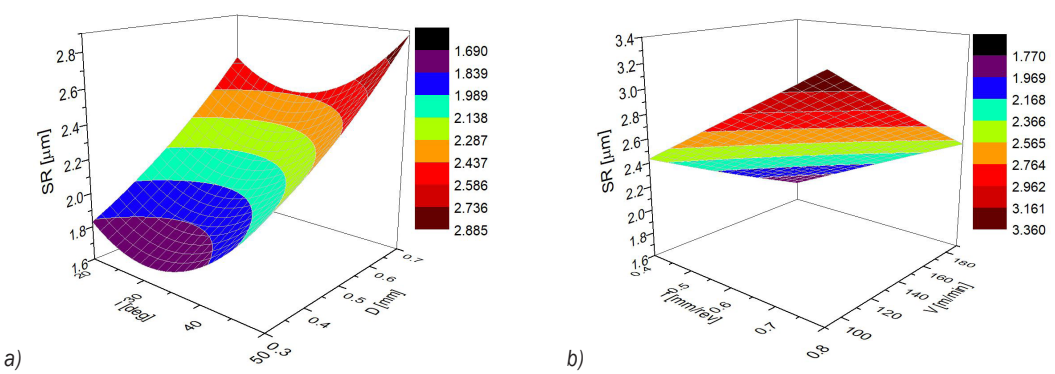

a) b)

Fig. 11. *Interactions of process parameters on the SR; a) SR vs. i and d, b) SR vs. V and f*

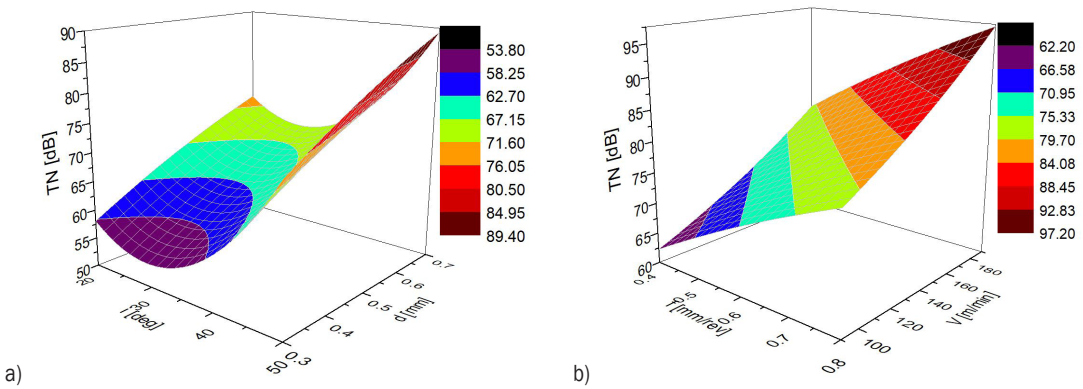

Fig. 12. *Interactions of process parameters on the TN; a) TN vs. A and D, b) TN vs. V and f*

The *TN* is increased by 27.6 % with an increment in the *d* (Fig. 12a). A higher *D* increases the material removal to be cut, leading to higher friction; hence, the *TN* increases. Moreover, a higher *d* causes greater resistance, resulting in higher turning noise.

The *TN* is increased by 28.2 % with an increment in the *f* (Fig. 12b). An increased *f* causes higher material removal to be cut, leading to higher friction; hence, the *TN* increases. Additionally, a higher *f* increases the machining power of the drive system; hence, a higher *TN* is produced.

The *TN* is increased by 29.3 % with an increment in the *V* (Fig. 12b). A higher *V* increases the engagement frequency of the spindle system; hence, the *TN* increases. Additionally, an increased *V* causes higher material removal to be cut, leading to higher friction; hence, the *TN* increases.

The E_t, *SR*, and *TN* are expressed as:

$$E_t = 0.43126 - 0.21181i + 14.09801d - 49.89973f - 0.25773V + 0.017943id - 0.04979if - 0.000085iV - 7.46871df - 0.03535dV + 0.05171 + 0.00374i^2 - 1.60143d^2 + 28.51704f^2 + 0.00064V^2 \quad (28)$$

$$SR = 3.29271 - 0.08815i - 0.4125d + 2.77125f - 0.0126V - 0.00666id + 0.00416if + 0.00006iV - 0.1875df + 0.00625dV - 0.00475fV + 0.00126i^2 + 1.58333d^2 - 0.07292f^2 + 0.0000053V^2 \quad (29)$$

$$TN = 56.38004 - 2.88317i + 57.05417d + 49.7375f - 0.00301V + 0.01666id + 0.275if - 0.0002iV - 8.125df + 0.0725dV + 0.0525fV + 0.04743i - 22.91667d^2 - 16.97917f^2 + 0.00044V^2 \quad (30)$$

4.4 Optimizing Outcomes Produced by the IQPSO

Table 9 shows the coefficients for turning objectives. The values of the *TU*, *SR*, and *TN* are presented in Table 10. The weight values of the *TE*, *SR*, and *TN* are 0.43, 0.37, and 0.20, respectively.

The Pareto fronts generated by IQPSO are exhibited in Fig. 13. As a result, turning objectives have contradictory trends. The reduction in the *SR* leads to a higher *TU* (Fig. 13a). Similarly, a decreased *TU* leads to a higher *TN* (Fig. 13b).

The TOPSIS is utilized to select the best point among feasible solutions. The optimum values of the *i*, *d*, *f*, and *V* are 35 deg, 0.30 mm, 0.40 mm/rev., and 190 m/min, respectively. The reductions in the *TE*, *SR*, and *TN* are 6.7 %, 22.3 %, and 23.5 %, respectively in comparison with the initial values (Table 11).

4.5 Comparisons with the Optimization Results Produced by the MOPSO

The optimum findings generated by the MOPSO of the *i*, *d*, *f*, and *V* are 29 deg, 0.30 mm, 0.40 mm/rev, and 172 m/min, respectively. The reductions in the *TU*, *SR*, and *TN* are 6.0 %, 20.9 %, and 23.0 %, respectively, as compared to the initial values. The number of feasible solutions generated by the IQPSO and MOPSO are 426 and 286, respectively. It can be stated that the IQPSO provides better optimization results than the MOPSO.

4.6 Evaluation of the Total Turning Cost

The comprehensive model for the *MC* is expressed as:

$$MC = k_e TU + k_c \frac{t_c}{T_T} + k_{labor}(t_o + t_{st} + t_a + t_{tc} + t_c) + k_{labor} t_{ch} \frac{t_c}{T_T} + \frac{(k_{fp} + k_{fd})(t_o + t_{st} + t_a + t_{tc} + t_c)V_u}{T_L} + \frac{(k_{md} + k_{mr})(t_o + t_{st} + t_a + t_{tc} + t_c)}{T_m} + \frac{k_n(t_o + t_{st} + t_a + t_{tc} + t_c)}{T_W}, \quad (31)$$

Table 9. *Experimental coefficients for the rotary turning process*

p_o [kW]	t_o [s]	P_{st} [kW]	t_{st} [s]	t_a [s]	t_{tc} [s]	A	α	β
0.48	4	0.72	6	8	8	16.2×105	2.65	0.27
γ	U_m [kJ/m³]	T_L [month]	V_{in} [cm³]	V_{ad} [cm³]	H [%]	ρ [g/cm³]	E_L [J/g]	U_m [kJ/m³]
0.37	9.16×103	1	8.5	4.5	5	0.92	422984	9.16x103

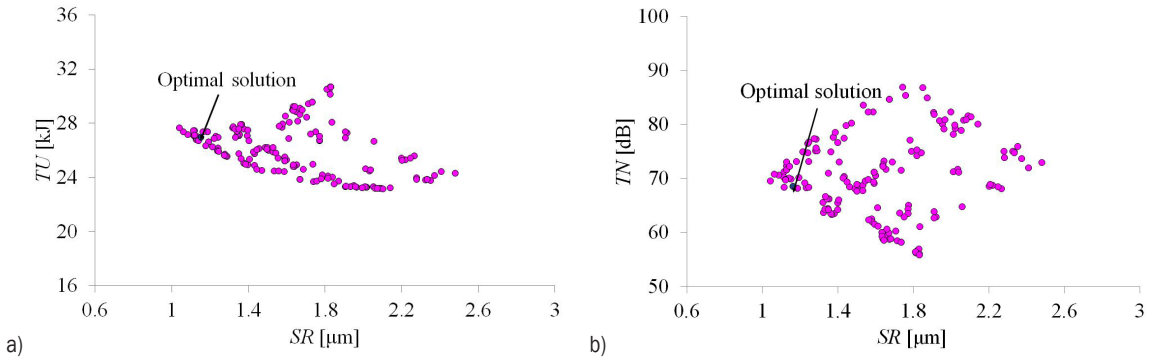

Fig. 13. *Pareto fronts generated by IQPSO; a) TE and SR, b) TN and SR*

Table 10. *The values of total energy consumption, average roughness, and turning noise*

No.	i [deg]	D [mm]	f [mm/rev]	V [m/min]	TU [kJ]	SR [μm]	TN [dB]
1	20	0.3	0.6	140	25.31	2.04	73.6
2	50	0.3	0.6	140	25.72	2.32	90.9
3	20	0.7	0.6	140	26.69	2.76	89.5
4	50	0.7	0.6	140	27.31	2.96	107.2
5	35	0.5	0.4	90	33.65	2.16	63.9
6	35	0.5	0.4	190	28.52	1.38	81.3
7	35	0.5	0.8	90	27.05	3.08	79.8
8	35	0.5	0.8	190	23.98	2.11	992
9	35	0.3	0.6	90	28.05	2.41	64.3
10	35	0.3	0.6	190	24.65	1.41	81.1
11	35	0.7	0.6	90	30.24	2.96	78.9
12	35	0.7	0.6	190	25.43	2.21	98.5
13	20	0.5	0.4	140	29.84	1.93	74.1
14	20	0.5	0.8	140	24.57	2.73	89.4
15	50	0.5	0.4	140	30.66	2.14	89.9
16	50	0.5	0.8	140	24.79	3.00	108.5
17	35	0.3	0.4	140	28.31	1.47	62.1
18	35	0.3	0.8	140	23.33	2.31	79.7
19	35	0.7	0.4	140	30.38	2.16	78.8
20	35	0.7	0.8	140	24.21	2.98	95.3
21	20	0.5	0.6	90	29.73	2.83	74.3
22	20	0.5	0.6	190	25.75	1.87	92.8
23	50	0.5	0.6	90	30.37	2.98	92.1
24	50	0.5	0.6	190	26.14	2.20	109.9
25	35	0.5	0.6	140	25.48	2.17	80.5
26	35	0.3	0.4	190	27.77	1.03	71.1

where k_e, k_c k_{labor} are the costs of energy, tool, and labour, respectively. V_u is the lubricant volume. k_{fp} and k_{fd} present the cost for the lubricant preparation and disposal, respectively. k_{md}, k_{mr}, and T_m are the cost of the degradation and remanufacturing for the lathe, respectively. T_m is the service life of the machine. k_n

Table 11. *The optimality produced by the IQPSO and MOPSO*

Method	i [deg]	d [mm]	f [mm/rev]	V [m/min]	TU [kJ]	SR [μm]	TN [dB]	S_i
Initial values	50	0.30	0.40	140	28.89	1.48	89.5	
Optimal values by IQPSO	35	0.30	0.40	190	26.95	1.15	68.5	0.8624
Reductions by IQPSO [%]					6.7	22.3	23.5	
Optimal values by MOPSO	29	0.30	0.40	172	27.08	1.17	68.9	
Improvement by MOPSO [%]					6.0	20.9	23.0	

Table 12. *Experimental coefficients for the turning cost model*

k_e [USD/kWh]	k_c [VND/piece]	k_{labour} [USD/h]	V_u [l]	k_{fp} [USD/l]	k_{fd} [USD/l]	T_L [month]	k_{md} [USD]	k_{mr} [USD]	T_m [year]	k_n [USD]
0.15	16.62	8.40	20	0.14	0.45	1	41244.75	1649.79	14	2.68

and T_w are the noise tax and working hours per month, respectively.

The empirical coefficients of the *MC* are shown in Table 12. It can be stated that, the *MC* is saved by 8.5 % at the selected point (Table 13).

Table 13. *Comparative values of the total cost*

Method	Optimization parameters				Response
	i [deg]	d [mm]	f [mm/rev]	V [m/min]	MC [USD]
Initial values	50	0.30	0.40	140	4.91
Optimal results	35	0.30	0.40	190	4.48
Reduction [%]					8.5

4.7 The Contribution Analysis

The proposed cutting tool could be used in the practical rotary turning process for other hard-to-cut alloys. The new rotary turning tool could be developed based on the current device.

The empirical correlations of the performance measures could be effectively employed to forecast the total energy, turned roughness, and noise emission.

The optimizing outcomes could be used in the practical operation to improve the technological data.

The proposed turning process could be applied to produce external surfaces for other difficult-to-cut alloys.

The develop optimization approach could be applied to deal with other issues of different machining operations.

The turning expense model could be used to compute total cost.

5 CONCLUSIONS

In the current work, the *TU*, *SR*, and *TN* of the rotary turning process were optimized, while optimal inputs were the *i*, *d*, *f*, and *V*. The MEREC and IQPSO were utilized to select optimal outcomes. The findings are expressed as below:

1. To save the *TU*, the low data of the *i* and *D* were used, while the highest data of the *f* and *V* were utilized. To decrease the *SR*, the low *d* and *f* were utilized, while the high *i* and *V* were employed. For reducing the *TN*, the lowest process parameters could be applied.
2. The *TU* and *SR* models were primarily affected by the *f* and *V*, followed by the *d* and *I*, respectively. For the *TN* model, the *V* had the highest contribution, followed by the *f*, *i*, and *d*, respectively.
3. The optimal *i*, *d*, *f*, and *V* were 35 deg, 0.30 mm, 0.40 mm/rev, and 190 m/min, respectively. The *TU*, *SR*, and *TN* were saved 6.7 %, 22.3 %, and 23.5 %, respectively.
4. The IQPSO provided better optimization outcomes for the rotary turning process, as compared to the MOPSO.
5. The *MC* was decreased by 8.5 % at the selected point.
6. The influences of rotary turning factors on the production rate and carbon emission will be explored in future works.

6 REFERENCES

[1] Karaguzel, U., Olgun, U., Uysal, E., Budak, E., Bakkal, M. (2015). Increasing tool life in machining of difficult-to-cut materials using nonconventional turning processes. *International Journal of Advanced Manufacturing Technology*, vol. 77, p. 1993-2004, **DOI:10.1007/s00170-014-6588-7**.

[2] Rao, T.B., Krishna, A.G., Katta, R.K., Krishna, K.R. (2015). Modeling and multi-response optimization of machining performance while turning hardened steel with self-propelled rotary tool. *Advances in Manufacturing*, vol. 3, p. 84-95, **DOI:10.1007/s40436-014-0092-z**.

[3] Teimouri, R., Amini, S., Mohagheghian, N. (2017). Experimental study and empirical analysis on effect of ultrasonic vibration

during rotary turning of aluminum 7075 aerospace alloy. *Journal of Manufacturing Processes*, vol. 26, p. 1-12, **DOI:10.1016/j.jmapro.2016.11.011**.

[4] Mohammad, L., Saeid, A., Mohsen, A. (2018). 3D FEM simulation of tool wear in ultrasonic assisted rotary turning. *Ultrasonics*, vol. 88, p. 106-114, **DOI:10.1016/j.ultras.2018.03.013**.

[5] Nguyen, T.T., Duong, Q.D., Mia, M. (2020). Sustainability-based optimization of the rotary turning of the hardened steel. *Metals*, vol. 10, art. ID 939, **DOI:10.3390/met10070939**.

[6] Nguyen, T.T. (2020). An energy-efficient optimization of the hard turning using rotary tool. *Neural Computing & Applications*, vol. 33, pp. 2621-2644, **DOI:10.1007/s00521-020-05149-2**.

[7] Umer, U., Kishawy, H., Abidi, M.H., Mian, S.H., Moiduddin, K. (2020). Evaluation of self-propelled rotary tool in the machining of hardened steel using finite element models. *Materials*, vol. 13, no. 22, art. ID 5092, **DOI:10.3390/ma13225092**.

[8] Ahmed, W., Hegab, H., Mohany, A., Kishawy, H. (2021). Analysis and optimization of machining hardened steel AISI 4140 with self-propelled rotary tools. *Materials*, vol. 14, no. 20, art. ID 6106, **DOI:10.3390/ma14206106**.

[9] Nieslony, P., Krolczyk, G., Chudy, R., Wojciechowski, S., Maruda, R., Biłous, P., Lipowczyk, M., Stachowiak, L. (2020). Study on physical and technological effects of precise turning with self-propelled rotary tool. *Precision Engineering*, vol. 66, pp. 62-75, **DOI:10.1016/j.precisioneng.2020.06.003**.

[10] Yujiang, L., Tao, C. (2021). Research on cutting performance in high-speed milling of TC11 titanium alloy using self-propelled rotary milling cutters. *International Journal of Advanced Manufacturing Technology*, vol. 116, p. 2125-2135, **DOI:10.1007/s00170-021-07592-4**.

[11] Ahmed, W., Hegab, H., Kishawy, H., Mohany, A. (2021). Estimation of temperature in machining with self-propelled rotary tools using finite element method. *Journal of Manufacturing Processes*, vol. 61, p. 100-110, **DOI:10.1016/j.jmapro.2020.10.080**.

[12] Chen, T., Wang, Y., Gao, W., Li, R. (2020). Comparative study on the cutting performance of self-propelled rotary cutters and indexable cutters in milling TC11 titanium alloy. *International Journal of Advanced Manufacturing Technology*, vol. 111, p. 2749-2758, **DOI:10.1007/s00170-020-06273-y**.

[13] Ahmed, W., Hegab, H., Mohany, A., Kishawy, H. (2021). On machining hardened steel AISI 4140 with self-propelled rotary tools: experimental investigation and analysis. *International Journal of Advanced Manufacturing Technology*, vol. 113, p. 3163-3176, **DOI:10.1007/s00170-021-06827-8**.

[14] Umer, U., Mian, S.H., Mohammed, M.K., Abidi, M.H., Moiduddin, K., Kishawy, H. (2022). Self-propelled rotary tools in hard turning: analysis and optimization via finite element models. *Materials*, vol. 15, no. 24, art. ID 8781, **DOI:10.3390/ma15248781**.

[15] Nguyen, T.T. (2021). Analytical approach-based optimization of the actively driven rotary turning for environmental and economic metrics considering energy footprint of materials. *Neural Computing & Applications*, vol. 33, p. 11937-11950, **DOI:10.1007/s00521-021-05891-1**.

[16] Nguyen, T.T., Duong, Q.D., Mia, M. (2021). Multi-response optimization of the actively driven rotary turning for energy efficiency, carbon emissions, and machining quality. *Proceedings of the Institution of Mechanical Engineers, Part B: Journal of Engineering Manufacture*, vol. 235, no. 13, p. 2155-2173, **DOI:10.1177/09544054211001014**.

[17] He, W., Xue, Z., Guo, R., Chen, N,. (2023). On machining K417 superalloy with sliding self-propelled rotary tools: simulation and experimental investigation. *International Journal of Advanced Manufacturing Technology*, vol. 126, p. 1669-1680, **DOI:10.1007/s00170-023-11218-2**.

[18] Sampath, B., Myilsamy, S. (2021). Experimental Investigation of a cryogenically cooled oxygenmist near-dry wire-cut electrical discharge machining process. *Strojniški vestnik - Journal of Mechanical Engineering*, vol. 67, no. 6, p. 322-330, **DOI:10.5545/sv-jme.2021.7161**.

[19] Ning, P., Zhao, J., Ji, S., Li, J., & Dai, H. (2021). Ultra-precision single-point diamond turning of a complex sinusoidal mesh surface using machining accuracy active control. *Strojniški vestnik - Journal of Mechanical Engineering*, vol. 67, no. 7-8, p. 343-351, **DOI:10.5545/sv-jme.2021.7172**.

[20] Tzotzis, A., García-Hernández, C., Huertas-Talón, J., Kyratsis, P. (2020). 3D FE modelling of machining forces during AISI 4140 hard turning. *Strojniški vestnik - Journal of Mechanical Engineering*, vol. 66, no. 7-8, p. 467-478, **DOI:10.5545/sv-jme.2020.6784**.

[21] Satheesh, C., Sevvel, P., Senthil Kumar, R. (2020). Experimental Identification of optimized process parameters for FSW of AZ91C Mg Alloy using quadratic regression models. *Strojniški vestnik - Journal of Mechanical Engineering*, vo. 66, no. 12, p. 736-751, **DOI:10.5545/sv-jme.2020.6929**.

[22] Ma, M., Xiong, W., Lian, Y., Han, D., Zhao, C., Zhang, J. (2019). Modeling and optimization for laser cladding via multi-objective quantum-behaved particle swarm optimization algorithm. *Surface and Coatings Technology*, vol. 381, art. ID 125129, **DOI:10.1016/j.surfcoat.2019.125129**.

[23] Tang, M., Zhu, W., Sun, S., Xin, Y. (2023). Mathematical modeling of resource allocation for cognitive radio sensor health monitoring system using coevolutionary quantum-behaved particle swarm optimization. *Expert Systems with Applications*, vol. 228, art. ID 120388, **DOI:10.1016/j.eswa.2023.120388**.

[24] Guo, F., Zhu, J., Huang, L., Li, H., Deng, J., Zhang, X., Wang, K., Liu, H., Hou, X. (2023). A modified BRDF model based on Cauchy-Lorentz distribution theory for metal and coating materials. *Photonics*, vol. 10, no. 7, art. ID 773, **DOI:10.3390/photonics10070773**.